Nilsson, A., Suttie, N., Korte, M., Holme, R., Hill, M. (2020): Persistent westward drift of the geomagnetic field at the core–mantle boundary linked to recurrent high-latitude weak/reverse flux patches. - Geophysical Journal International, 222, 2, 1423-1432.

https://doi.org/10.1093/gji/ggaa249

Geophysical Journal International

Geophys. J. Int. (2020) **222,** 1423–1432
Advance Access publication 2020 May 20
GJI Geomagnetism, Rock Magnetism and Palaeomagnetism

doi: 10.1093/gji/ggaa249

Persistent westward drift of the geomagnetic field at the core–mantle boundary linked to recurrent high-latitude weak/reverse flux patches

Andreas Nilsson,[1] Neil Suttie,[1] Monika Korte,[2] Richard Holme[3] and Mimi Hill[3]

[1] *Department of Geology, Lund University, Sölvegatan 12, 22362 Lund, Sweden. E-mail: andreas.nilsson@geol.lu.se*
[2] *GFZ German Research Centre for Geosciences, Telegrafenberg, 14473 Potsdam, Germany*
[3] *Department of Earth, Ocean and Ecological Sciences, University of Liverpool, Oliver Lodge Laboratories, Oxford Street, Liverpool L69 7ZE, UK*

Accepted 2020 May 14. Received 2020 May 13; in original form 2019 December 18

SUMMARY

Observations of changes in the geomagnetic field provide unique information about processes in the outer core where the field is generated. Recent geomagnetic field reconstructions based on palaeomagnetic data show persistent westward drift at high northern latitudes at the core–mantle boundary (CMB) over the past 4000 yr, as well as intermittent occurrence of high-latitude weak or reverse flux patches. To further investigate these features, we analysed time-longitude plots of a processed version of the geomagnetic field model pfm9k.1a, filtered to remove quasi-stationary features of the field. Our results suggest that westward drift at both high northern and southern latitudes of the CMB have been a persistent feature of the field over the past 9000 yr. In the Northern Hemisphere we detect two distinct signals with drift rates of 0.09° and 0.25° yr^{-1} and dominant zonal wavenumbers of $m = 2$ and 1, respectively. Comparisons with other geomagnetic field models support these observations but also highlight the importance of sedimentary data that provide crucial information on high-latitude geomagnetic field variations. The two distinct drift signals detected in the Northern Hemisphere can largely be decomposed into two westward propagating waveforms. We show that constructive interference between these two waveforms accurately predicts both the location and timing of previously observed high-latitude weak/reverse flux patches over the past 3–4 millennia. In addition, we also show that the 1125-yr periodicity signal inferred from the waveform interference correlates positively with variations in the dipole tilt over the same time period. The two identified drift signals may partially be explained by the westward motion of high-latitude convection rolls. However, the dispersion relation might also imply that part of the drift signal could be caused by magnetic Rossby waves riding on the mean background flow.

Key words: Core; Magnetic field variations through time; Palaeomagnetic secular variation; Palaeomagnetism.

1 INTRODUCTION

Earth's magnetic field is believed to be generated by convection in Earth's iron-rich liquid outer core, a process known as the geodynamo. Observed changes of the geomagnetic field, also known as secular variation, have the potential to constrain the processes responsible for maintaining it. As early as the 17th century, Halley (1692) noted that specific features of the geomagnetic field at Earth's surface appear to drift predominantly in a westward direction. By calculating the drift rate around latitudinal circles, Bullard *et al.* (1950) inferred a global average rate of 0.18° yr^{-1} for the westward drift of the non-dipolar field at Earth's surface over the period 1907–1945.

With the development of geomagnetic field models designed to map the field at the core–mantle boundary (CMB), Bloxham & Gubbins (1985) established that the westward drift is not a global phenomenon but mainly restricted to the region between 90° E and 90° W. By studying the non-axisymmetric flux at the core, Finlay & Jackson (2003) showed that the observed drift is most prominent in the equatorial region, with westward motion of flux at a rate of 17 km yr^{-1} (equivalent to 0.27° yr^{-1}) persisting throughout the past four centuries. Westward drift is also observed at high latitudes, with (south)west movement of an intense flux patch beneath Patagonia over the same time period and more recently the accelerated westward motion (up to 0.90° yr^{-1}) of an intense flux patch beneath Canada, potentially associated with a high-latitude jet (Livermore *et al.* 2017). All of these observations are consistent with, or can at least partially be explained by, a giant westward drifting eccentric planetary gyre (Barrois *et al.* 2018), originally isolated in core flow inversions by Pais & Jault (2008). This planetary gyre has been

successfully reproduced in numerical dynamo simulations involving both gravitational coupling of the inner core to the mantle and differential inner core growth causing preferential buoyancy release in the outer core beneath the Indian Ocean (Aubert *et al.* 2013).

An alternative hypothesis for the observed westward drift, originally proposed by Hide (1966), involves the propagation of magnetohydrodynamic waves. According to this theory, the horizontal velocity of the fluid is not necessarily the same as the westward drift velocity. Rotating magnetic–Coriolis waves are split into two classes, fast 'inertial' modes and slow 'magnetic' modes, with the latter operating on timescales of 100–10 000 yr (Finlay *et al.* 2010). Hide (1966) investigated a specific quasi-geostrophic (i.e. with little variation in the z-direction) form of the slow magnetic–Coriolis waves, often called magnetic Rossby waves, which he found were likely to contribute to secular variation. These waves propagate westwards and are dispersive (shorter wavelengths have faster phase velocities). Hori *et al.* (2015, 2018) recently demonstrated that westward drifts in dynamo simulations, similar to those observed over the past four centuries, could be explained by such magnetic Rossby waves riding on mean flow advection. Various excitation mechanisms have been proposed that could produce these waves, including turbulence in the core (Hide 1966), topographic differences at the CMB (Hide 1966) or even length-of-day (LOD) variations through topographic core–mantle coupling (Yoshida & Hamano 1993).

Investigations of azimuthal motions in geomagnetic field models constrained by palaeomagnetic data have shown evidence for both eastward and westward drifts (Dumberry & Finlay 2007; Wardinski & Korte 2008; Amit *et al.* 2011; Nilsson *et al.* 2014; Hellio & Gillet 2018). The azimuthal motions in the field are most clearly seen at mid- to high northern latitudes, linked to movements of intense flux patches at the CMB (Dumberry & Finlay 2007), which is likely a reflection of structures that can be resolved by these models. Based on the (now superseded) CALS7K.2 model, Dumberry & Finlay (2007) and Wardinski & Korte (2008) observed more or less equal occurrence of eastward and westward drifts, with typical drift rates of $\pm$ 0.15° yr^{-1} at 40°–60° N. Amit *et al.* (2011) based their analysis on the CALS3K.3 model (Korte *et al.* 2009), using an algorithm to identify and track movements of intense (normal polarity) flux patches found mostly around the edge of the inner core tangent cylinder. They also observed both eastward and westward motions with average drift rates around 0.20° yr^{-1}, although westward drift was slightly more common. Studies based on more recent geomagnetic field reconstructions (Nilsson *et al.* 2014; Hellio & Gillet 2018), however, show a clear dominance of westward drift over the past 4000 yr with drift rates of 0.20–0.25° yr^{-1} reported by Hellio & Gillet (2018) and persistent slow drift rates of $\sim$0.07° yr^{-1} (equivalent to a 5000-yr rotation period) reported by Nilsson *et al.* (2014).

In addition to persistent westward drift, Nilsson *et al.* (2014) also noted the intermittent occurrence (1500BC, 300BC, 700AD, 1900AD) of weak or reversed flux patches at high northern latitudes at the CMB, potentially originating at low latitudes and migrating polewards. Campuzano *et al.* (2019) described in more detail the evolution of the most recent of these high-latitude weak/reverse flux patches. They find that the flux patch emerged at the equator in the Atlantic hemisphere around 1000–1400 AD and moved north-eastward at a rate of 10 km yr^{-1}. They further note that the evolution of this flux patch was more or less antisymmetric to the simultaneous south-westward migration of another reverse flux patch associated with the development of the South Atlantic Anomaly (SAA), suggesting that these observations could be linked. However, similar hemispherical asymmetries have not been observed for the other occurrences of high-latitude weak/reverse flux.

Attempts have also been made to identify and track movements of reverse flux patches. Based on the method of Amit *et al.* (2011), Terra-Nova *et al.* (2015) noted that reverse flux patches mostly exhibit westward drift and generally migrate toward higher latitudes. Terra-Nova *et al.* (2015) also concluded that the detection of reverse flux patches is strongly dependent on spherical harmonic degrees 4 and above, which is at the limit of what current palaeomagnetic field models can robustly resolve, particularly in the Southern Hemisphere of the core (Nilsson *et al.* 2014).

Overall, the observations of azimuthal motions and reverse flux patches in the palaeomagnetic record vary significantly between different studies. The discrepancies can largely be explained by differences between the geomagnetic field models (many of which are now superseded) rather than the methods used to analyse the data (e.g. Terra-Nova *et al.* 2016). A range of new millennial scale geomagnetic field models has been produced over the past few years (Nilsson *et al.* 2014; Pavón-Carrasco *et al.* 2014; Constable *et al.* 2016; Hellio & Gillet 2018; Arneitz *et al.* 2019; Campuzano *et al.* 2019). These models are based on more or less the same data compilation, which has been vastly improved from the earliest versions, for example used to constrain CALS7K.2 (Korte *et al.* 2005). This data compilation typically includes archaeomagnetic data from GEOMAGIA50.v3 database (Brown *et al.* 2015), which is continually updated, and in some cases sedimentary data compiled by Korte *et al.* (2011) and later augmented by Panovska *et al.* (2015). Overall the agreement between the different palaeomagnetic field models has improved, but significant differences still exist. The most important difference between these models can be traced to the choices of how to treat sedimentary data, which if included will improve data coverage while also leading to smoother models, for example due to post-depositional processes (Nilsson *et al.* 2018). Different strategies of how to address data uncertainties and outliers and how much weight is given to different data types (e.g. sedimentary data) also have potentially large impacts on the resulting models.

The main objective of this study is to investigate the persistence of westward drift at the CMB on Holocene timescales and whether or not this is linked to the occurrence of reverse flux at high northern latitudes. The analyses will primarily be based on the pfm9k.1a model, which uses a crude Bayesian approach to synchronize timescales of different sediment records based on the palaeomagnetic data (Nilsson *et al.* 2014). To evaluate how robust our observations are, we compare our results with similar analyses on models constructed using different modelling strategies and data as well as different models from the same model family.

2 METHODS

2.1 Time-longitude plots

To investigate eastward and westward drifts, we use so-called time-longitude (TL) plots, calculated with a 2° and 10-yr grid size, and follow the approach of Finlay & Jackson (2003) and Dumberry & Finlay (2007). First we remove the time-averaged axisymmetric part of the field and then high-pass filter the Gauss coefficients with a cut-off frequency of 1/2500 yr^{-1}. The cut-off frequency, similar to 1/2000 yr^{-1} used by Dumberry & Finlay (2007), was

found to be enough to filter out quasi-stationary field structures without removing too much of the original signal. We estimate that the residual field captures 52 per cent of the variability of the original radial field (B_r) at the CMB (see Supporting Information). The filtered model is given the suffix '_p' to distinguish it from the original model. To avoid end-effects related to the zero-phase Butterworth filter we remove 300 yr at the beginning and end of the model. Although pfm9k.1a model covers the time period 7500 BC–2000 AD, it was only intended to be used for the period 7000 BC–1900 AD and we therefore restrict our analyses to the period 7000 BC–1700 AD.

2.2 Radon drift determination

To quantitatively estimate the azimuthal drift rates observed in the TL plots we use a technique based on Radon transform (for more details see, Finlay & Jackson 2003; Dumberry & Finlay 2007). The Radon transform of a 2-D TL image provides a measure of the amount of coherent signal found along different angles of the image, which directly translates to different azimuthal drift rates. In addition to Radon drift determinations of TL plots at latitudes from 70° S to 70° N, we calculated drift rates based on Radon transforms for pfm9k.1a_p at 60° N over 2500-yr moving windows at 100-yr time steps. The resulting so-called time-drift plots, with the signal power in each window normalized to the maximum value, are useful to investigate the persistence over time of observed high-latitude westward drift.

2.3 Frequency–wavenumber analysis

To further investigate the identified drift rates, we use 2-D frequency–wavenumber power spectra of the TL plots at 60° N, where the strongest drifts occur, which were calculated using fast Fourier transform. Peaks in these power spectra identify dominant zonal wavenumbers $m = 360°/\lambda$ (where λ is the angular wavelength) and frequencies $f = 1/T$ (where T is the period in years). Based on the time-drift plots from the Radon transform, we calculated the frequency–wavenumber power spectra for three partially overlapping time windows; 2000BC–1700AD, 5000–1000BC and 7000–4000BC. In the following, unless explicitly specified, we adopt the convention of expressing frequencies and drift rates as negative (positive) for westward (eastward) propagation directions.

3 RESULTS

3.1 Analysis of the past 9000 yr from the pfm9k.1a model

TL plots at 60° N, of the original model (pfm9k.1a) and filtered model (pfm9k.1a_p) are shown in Fig. 1. We chose 60° N as this is where the high-latitude intense flux patches are mainly seen and, as we will see from the Radon transform results, also where the strongest azimuthal drift rates are observed. The TL plots show mostly evidence for westward drift, manifested as diagonal lines going from the bottom right to top left. Eastward drift is also observed (e.g. around 2000–1000BC; −90–0° E), but these features appear to be less continuous in time. The filtered version (Fig. 1b) shows drift signatures much more clearly, so we focus on that in the following. Moreover, to better illustrate slow drift we extend the longitudinal range to −360° to 360°, that is showing two duplicate TL plots next to each other in that panel.

We distinguish at least two different westward drift rates, (i) a slow $-0.09°\ \mathrm{yr}^{-1}$ (corresponding to 2.7 km yr^{-1}) drift superimposed by a (ii) faster $-0.25°\ \mathrm{yr}^{-1}$ (7.6 km yr^{-1}) propagating signal, marked by the dashed–dotted and dashed lines respectively in the figure. The slow westward drift rate is similar to the $-0.07°\ \mathrm{yr}^{-1}$ drift (corresponding to a 5000-yr rotation period) previously noted by Nilsson *et al.* (2014) over the past 4000 yr. However, after high-pass filtering the model we find evidence that this slow westward drift has been persistent throughout the past 9000 yr. The faster drift rate is consistent with classic westward drift originally proposed by Bullard *et al.* (1950) and recently noted by Hellio & Gillet (2018) in their model COV-LAKE covering similar timescales.

The lines in Fig. 1(b) (and Fig. 1a) have deliberately been plotted along transects of positive residual field (corresponding to weak or reverse flux in the unfiltered model; Fig. 1a) where the drift signal appears to be stronger. The drift lines are only continuous, indicating movement of a single flux patch, over shorter time periods. In general, the observed drift lines are rather patchy, consistent with a stop-and-go motion described by Nilsson *et al.* (2014) or a preferred location/configuration of flux. The faster drift signal is mostly visible in the Pacific hemisphere between 90° and 270° E. We also note a general occurrence of more intense flux around 0°, 90°, 180°, and 270° E, suggesting the potential presence of one or two standing waves.

In Fig. 2(a), we show the results from Radon transform of TL plots at latitudes from 70° S to 70° N for pfm9k.1a_p. As previously stated, the strongest (dominantly westward) drift rates are observed at high northern latitudes, around 60° N, with two distinct drift rates ($-0.09°$ and $-0.25°\ \mathrm{yr}^{-1}$) being resolved. The analysis also reveals dominant westward drift ($-0.22°\ \mathrm{yr}^{-1}$) at high southern latitudes, around 60° S, as well as notable peaks in signal power associated with eastward drift ($\sim 0.15°\ \mathrm{yr}^{-1}$) at northern mid-latitudes.

The results of the time-drift plots shown in Fig. 2(b) indicate persistent westward drift at 60° N throughout the past 9000 yr. There is a strong $\sim 0.09°\ \mathrm{yr}^{-1}$ westward drift signal present for most of the record with faster westward drift rates ($\sim 0.25°\ \mathrm{yr}^{-1}$) appearing around 3000BC and onwards. In the earliest few time windows the two signals appear to merge into a single peak around $-0.20°\ \mathrm{yr}^{-1}$.

The frequency–wavenumber spectra for the three overlapping time intervals at 60° N are shown in Figs 3(a)–(c). For the first time window (2000 BC–1700 AD) the power spectra show westward propagating waves with dominant zonal wavenumbers of $m = 1$ and 2. This is consistent with the two identified drift rates being described by an $m = 2$ waveform ($f = -1/2000\ \mathrm{yr}^{-1}$ with drift rate $d = \lambda f = -0.09°\ \mathrm{yr}^{-1}$) and an $m = 1$ waveform ($f = -1/1440\ \mathrm{yr}^{-1}$ with drift rate $d = \lambda f = -0.25°\ \mathrm{yr}^{-1}$) respectively (see stars in Fig. 3a as well as the dashed–dotted and dashed lines in Fig. 1). We also find a weak $m = 2$ signal in eastward direction around $f = 1/2000\ \mathrm{yr}^{-1}$ (as well as $f = 1/1000\ \mathrm{yr}^{-1}$), which would be expected from the presence of a standing wave, previously mentioned.

From 5000 to 1000 BC, the $m = 1$ waveform (representing the faster drift rates) is more or less absent, which is consistent with the observations from time-drift plot in Fig. 2(b). The weaker $m = 2$ eastward drift signal also persists at similar frequencies. In the earliest time window (7000–4000 BC), the strongest signal is found at an intermediate frequency around $f \approx -1/1800\ \mathrm{yr}^{-1}$ with zonal wavenumber $m = 1$, which corresponds to the $-0.20°\ \mathrm{yr}^{-1}$ drift rates observed in Fig. 2(b).

In Fig. 3(d), we show the frequency–wavenumber spectrum of the TL plot at 60° S latitude over the first time window (2000 BC–1700 AD). The strongest signal is associated with a westward propagating $m = 1$ waveform at frequency $f \approx -1/1650\ \mathrm{yr}^{-1}$, which is

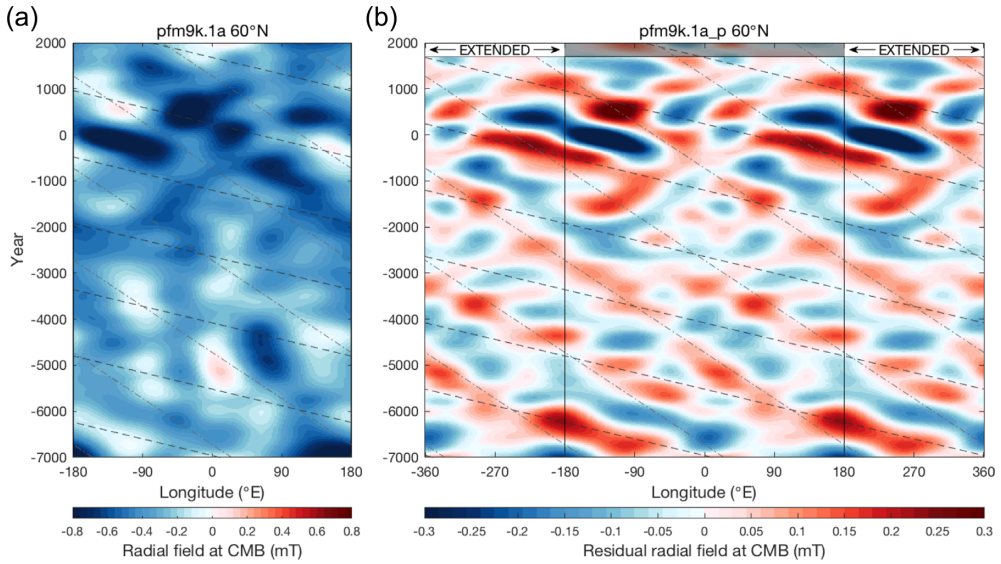

Figure 1. TL plots (60°N) of the radial field at the CMB predicted by (a) pfm9k.1a and (b) pfm9k.1a_p, with the axisymmetric part of the field removed and high-pass filtered with cut-off frequency of 1/2500 yr^{-1}. The first and last 300 yr of the filtered model were not considered during the analyses due to end-effects associated with the filtering process. Dotted–dashed diagonal grey lines correspond to westward drift at rates of -0.09° yr^{-1} ($f = -1/2000$ yr^{-1}, $m = 2$) and dashed grey lines correspond to drift rates of -0.25° yr^{-1} ($f = -1/1440$ yr^{-1}, $m = 1$).

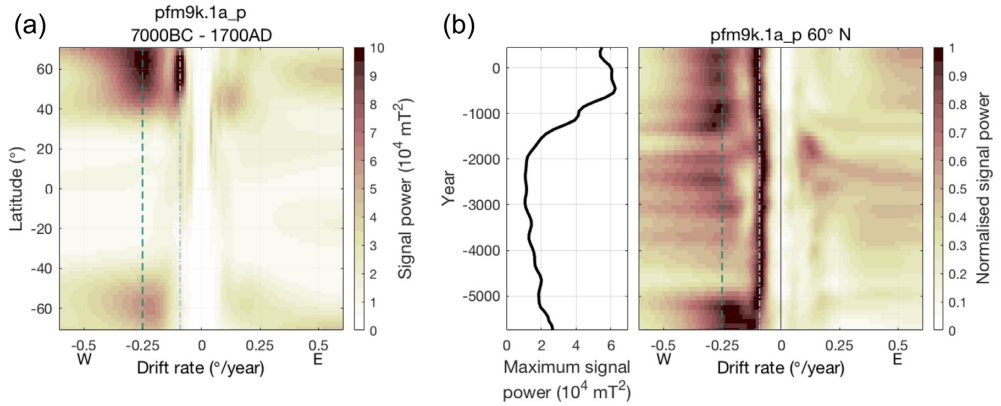

Figure 2. (a) Radon drift determination on TL plot of pfm9k.1a_p over the time period 7000 BC–1700 AD. The radon drift determination was performed for latitudes 70° S to 70° N at 2° increments. The temporal and spatial resolution for each TL plot was 10 yr and 2°. Vertical green dashed and light blue dotted–dashed lines denote westward rift rates of -0.25° and -0.09° yr^{-1}, respectively. (b) Radon drift determination on TL plots of pfm9k.1a_p at 60° N over a 2500-yr moving window (100 yr increments). The signal power is normalized to the maximum signal power (thick black line) in each time window. Vertical green dashed and light blue dotted–dashed lines denote westward rift rates of -0.25° and -0.09° yr^{-1}, respectively.

consistent with the single peak in drift rates at high southern latitudes of -0.22° yr^{-1} determined using the Radon transform method (Fig. 2a).

3.2 Effects of model resolution

The resolution of pfm9k.1a at the CMB varies spatially (and temporally) due to the uneven distribution of the palaeomagnetic data used to constrain the model (e.g. more than 88 per cent of the data come from the Northern Hemisphere). Based on comparisons with the *gufm1* model, Nilsson *et al.* (2014) estimated that the pfm9k.1a model resolution at 1900 AD is roughly equivalent to a spherical harmonic truncation at degrees 5–6 in the Northern Hemisphere and degrees 3–4 in the Southern Hemisphere. These truncation levels could probably be regarded as upper limits for the full 9000-year range of the model. The low model resolution at high southern latitudes limits the waveform structures we can expect to resolve in this region but could also lead to a distortion of the signal due to aliasing effects.

To demonstrate this we performed the same analyses as in Section 3.1 on a low-resolution version of the pfm9k.1a model, truncated at spherical harmonic degree 4 (pfm9k.1a[$l_{max} = 4$]). In Figs 4(a) and (b), respectively, we show the results of both the Radon drift determination (7000 BC–1700 AD) and the frequency–wavenumber spectrum of the TL plot at 60° N (2000 BC– 700 AD) based on the truncated pfm9k.1a, filtered in the same way as the original model. The Radon drift determination of the truncated model (Fig. 4a) fails to distinguish the two drift rates at high northern latitudes (Fig. 2a) and instead only shows a single peak. Similar to our observations for 60° S in the original model, the truncated model does not show any $m = 2$ structures at 60° N but instead shows a broad peak at zonal wavenumber $m = 1$ covering the frequency range of the previously proposed waveforms (Fig. 4b).

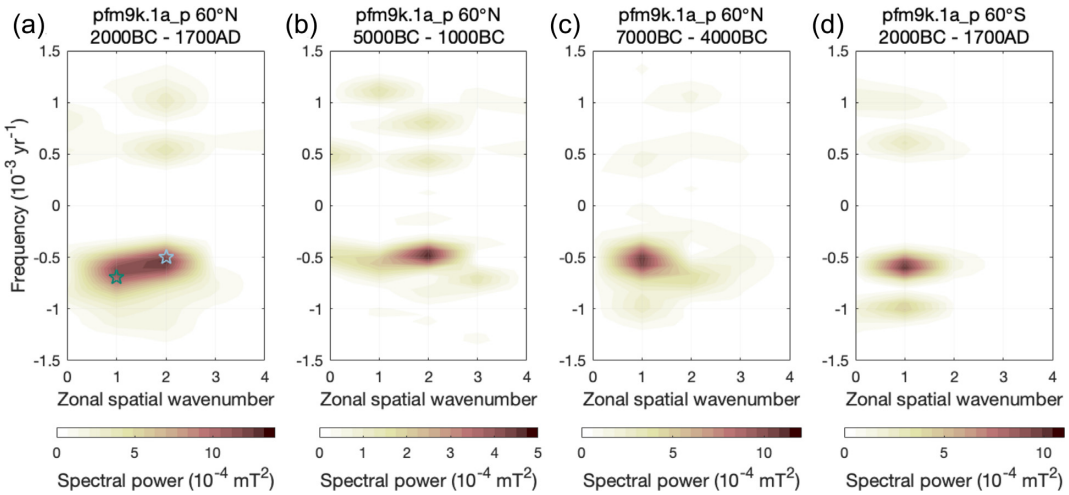

Figure 3. Frequency–wavenumber spectra of TL plots based on pfm9k.1a_p at 60° N over time periods (a) 2000 BC–1700 AD, (b) 5000–1000 BC, (c) 7000–4000 BC and (d) at 60° S over 2000 BC–1700 AD. The light blue star, frequency $f = -1/2000$ yr^{-1} and zonal wavenumber $m = 2$, and green star, frequency $f = -1/1440$ yr^{-1} and zonal wavenumber $m = 1$, are shown for reference only. Positive (negative) frequencies indicate eastward (westward) drift.

This comparison implies that the observed differences between the Northern and Southern Hemisphere drift signals could be explained by spatial variations in the model resolution. However, a visual comparison between the TL plots at 60° S of the original model and at 60° N of the truncated model (see Fig. S2, Supporting Information) also reveals that the detected signals drift in and out of phase with each other, suggesting that model resolution can only explain part of the differences. We also note that the largely comparable observations at 60° N from the early part of pfm9k.1a_p, that is $-0.20°$ yr^{-1} drift rates dominated by zonal wavenumbers $m = 1$ (Figs 2b and 3c), suggest that the lack of two distinct signals in this time period could potentially also be related to limited model resolution due to the decrease in data density with increasing time. In the same way that the model resolution in the Southern Hemisphere limits (and potentially distorts) what we can detect we should also expect that the model resolution in the Northern Hemisphere probably prevents us from detecting anything beyond zonal wavenumber $m = 2$.

3.3 Model comparison

To investigate the robustness of our observations, so far based only on pfm9k.1a_p, we applied the Radon drift determination to different models constructed with different modelling strategies and data (Figs 5a–d) as well as to different models within the same model family (Figs 5e–g). Note that for COV-LAKE and COV-ARCH, which consist of ensembles of models, the suffix '_M' is added to highlight that the results are based on the mean model.

In all cases, except for COV-ARCH_M_p which is the only model that excludes sedimentary data, we find strong signals associated with the two distinct westward drift rates at high northern latitudes as identified in pfm9k.1a_p. In COV-ARCH_M_p at similar latitudes, we find a peak around $-0.22°$ yr^{-1} and only a weak signal associated with the $-0.09°$ yr^{-1} drift rates. Similarly to the Southern Hemisphere signal in pfm9k.1a_p, the frequency–wavenumber spectrum for COV-ARCH_M_p is dominated by $m = 1$ structures (see Fig. S5, Supporting Information). This is likely due to the lack of archaeomagnetic data at high northern latitudes, reducing the spatial resolution of the model in this region of the CMB and the ability to resolve $m = 2$ structures (see Section 3.2).

All three models that include sedimentary data show elevated drift signals at high southern latitudes. The dominance of westward drift, observed in pfm9k.1a_p, is reproduced in two models (Figs 5b and c), with peaks around similar drift rates ($-0.22°$ yr^{-1}). We note that in these two models the observed westward drift at 60° S is associated with zonal wavenumbers $m = 1$ (see Supporting Information), similarly to pfm9k.1a_p. The absence of corresponding strong drift signals at high southern latitudes in COV-ARCH_M_p is perhaps not surprising given the general lack of archaeomagnetic data from this region. In addition to the observed high-latitude westward drift, two models (Figs 5a and c) also show support for eastward drift at northern mid-latitude, previously identified in pfm9k.1a_p.

To compare Radon drift determinations between models from the same model families we focus on latitude 60° N (Figs 5e–g). Of the investigated model families there are three bootstrap models available: pfm9k.1b, COV-LAKE and COV-ARCH. It is worth noting that the pfm9k.1a model is not the same as the average model of pfm9k.1b but could rather be regarded as one of the most likely draws from this ensemble due to the synchronization of the individual sediment timescales. We find good support for the $0.09°$ yr^{-1} westward drift signal in both pfm9k.1b and COV-LAKE but not in COV-ARCH, which is consistent with the observations from the model average. Elevated signal power around drift rates $-0.25°$ yr^{-1} are present in most of COV-LAKE and COV-ARCH, but only weakly represented in pfm9k.1b. The lack of a clear $-0.25°$ yr^{-1} signal in pfm9k.1b, compared to pfm9k.1a, shows how sensitive these observations are to age uncertainties in sedimentary data. In all three model families, there is also support for weaker eastward drift with similar rates.

4 DISCUSSION

4.1 Potential sources for the detected high-latitude westward drift at the CMB

We have shown, based on the pfm9k.1a model, that azimuthal motions at high northern latitudes of the CMB over the past 9000 yr are dominated by westward drift concentrated to two distinct rates ($-0.09°$ and $-0.25°$ yr^{-1}). While the slow drift rates have remained a persistent feature over most of the studied time interval, the faster

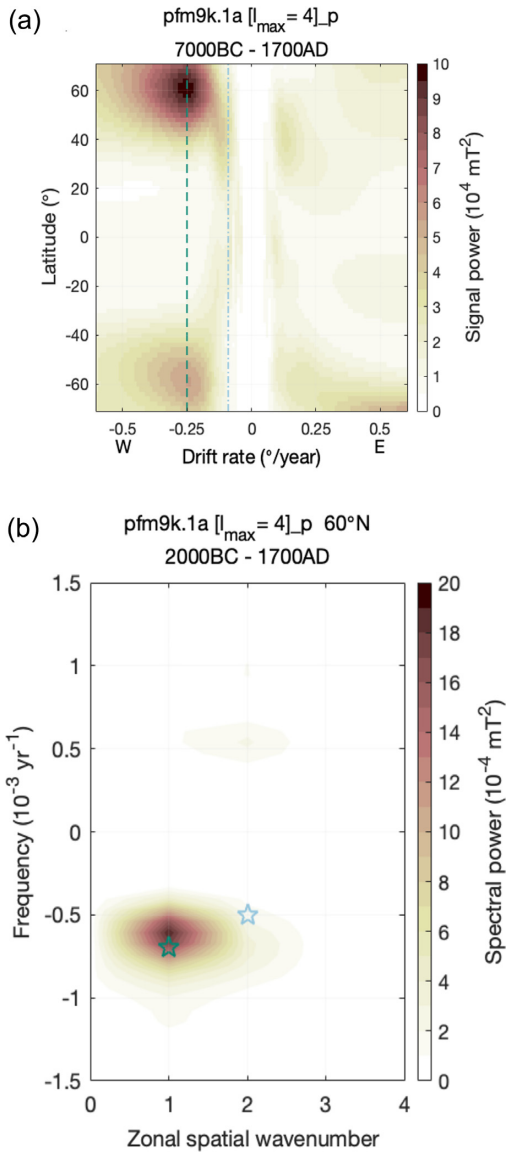

Figure 4. (a) Radon drift determination on TL plot of pfm9k.1a[$l_{max} = 4$]_p (pfm9k.1a truncated at spherical harmonic degree 4) over the time period 7000 BC–1700 AD. The radon drift determination was performed for latitudes 70° S to 70° N at 2° increments. The temporal and spatial resolution for each TL plot was 10 yr and 2°. Vertical green dashed and light blue dotted–dashed lines denote westward rift rates of $-0.25°$ and $-0.09°$ yr^{-1} respectively. (b) Frequency–wavenumber spectra of TL plots over the time period 2000 BC–1700 AD at 60° N based on pfm9k.1a[$l_{max} = 4$]_p. The light blue stars, frequency $f = -1/2000$ yr^{-1} and zonal wavenumber $m = 2$, and green stars, frequency $f = -1/1440$ yr^{-1} and zonal wavenumber $m = 1$, are shown for reference only. Positive (negative) frequencies indicate eastward (westward) drift.

drift rates appear to wax and wane with strong signals detected around 7000–6000 BC and during the last 3–4 millennia (see Figs 1 and 2). We also find evidence for dominant strong westward drift ($-0.22°$ yr^{-1}) at high southern latitudes, but limitations with the model resolution prevents direct comparisons with the Northern Hemisphere observations. Comparisons between different models support the conclusions from pfm9k.1a but also highlight how sensitive these observations are to the distribution and uncertainties of the data used to constrain the models. Based on these results we therefore restrict the following discussion to observations from the Northern Hemisphere and the past 3–4 millennia.

The observed drift is dominated by zonal wavenumbers $m = 2$ and 1. The $m = 2$ signal essentially describes a slow westward motion of two intense high-latitude flux patches, previously noted by Nilsson *et al.* (2014) for the past 4000 yr. This could be interpreted as representing high-latitude convection rolls (Gubbins & Bloxham 1987) carried along by the mean zonal flow in the core. As shown in the TL plot in Fig. 1, this pattern is only partly explained by continuous movement of individual flux patches and more generally generated by the appearance and disappearance of flux, for example migrating from lower or higher latitudes (or indeed from east or west). This would explain why similar patterns have gone largely unnoticed by other approaches designed to track the movements of individual flux patches (Amit *et al.* 2011; Terra-Nova *et al.* 2015; Terra-Nova *et al.* 2016). Such discontinuities of flux movements at the CMB will likely arise as an effect of chronologic data uncertainties (Nilsson *et al.* 2014), but it is perhaps also unlikely that individual flux patches remain intact/underformed over long timescales.

The observed $m = 1$ drift rate is of the same magnitude as the classic westward drift (Bullard 1950) and most likely the same signal as previously observed by Dumberry & Finlay (2007) and Hellio & Gillet (2018). The fact that the two detected drift rates shows a dispersive relationship (Fig. 3a) indicates that one or both could, at least partially, be generated by magnetic Rossby waves. Such waves are expected to be mostly relevant at high latitudes as investigated here (Hori *et al.* 2015). However, the observed dispersion relation, with longer ($m = 1$) wavelengths propagating with faster phase velocity, is opposite to the predicted dispersion for magnetic Rossby waves (Hide 1966). One interpretation is that the $m = 1$ signal represents a wave riding on the mean background flow, represented by the $m = 2$ signal as suggested above. This would suggest a wave propagation speed of $-0.16°$ yr^{-1}, after subtracting the background flow.

An alternative explanation may be provided by the forced magnetohydrodynamic waves proposed by Yoshida & Hamano (1993), which are expected to result in secular variation frequencies independent of zonal wavenumber. Such waves are hypothesized to be generated by variations in LOD that induce flow in the core due to topographic differences of the CMB. In their model, the frequency of the secular variation is the same as that of the external forcing, that is the variations in LOD. Interestingly, millennial-scale reconstructions of LOD based on historical records of solar and lunar eclipses (Morrison & Stephenson 2001) show variations on similar timescales as the detected drift rates and have previously also been shown to correlate with changes in the dipole tilt (Nilsson *et al.* 2011).

4.2 Wave interference and occurrence of high-latitude weak/reverse flux

As shown in Fig. 3(a), the observed westward drift at 60° N over the past 4000 yr can largely be decomposed into two waveforms, represented by the two stars in the figure. To further examine the interference pattern predicted by the inferred waveforms we construct a simple model composed of two sinusoidal waves of the form

$$W(\phi, t) = \cos(m\phi - \omega t)$$

where ϕ = longitude, t = time and $\omega = 2\pi f$ is the angular frequency of the waves (with angles given in radians). The superposition of the two waves gives rise to an interference pattern

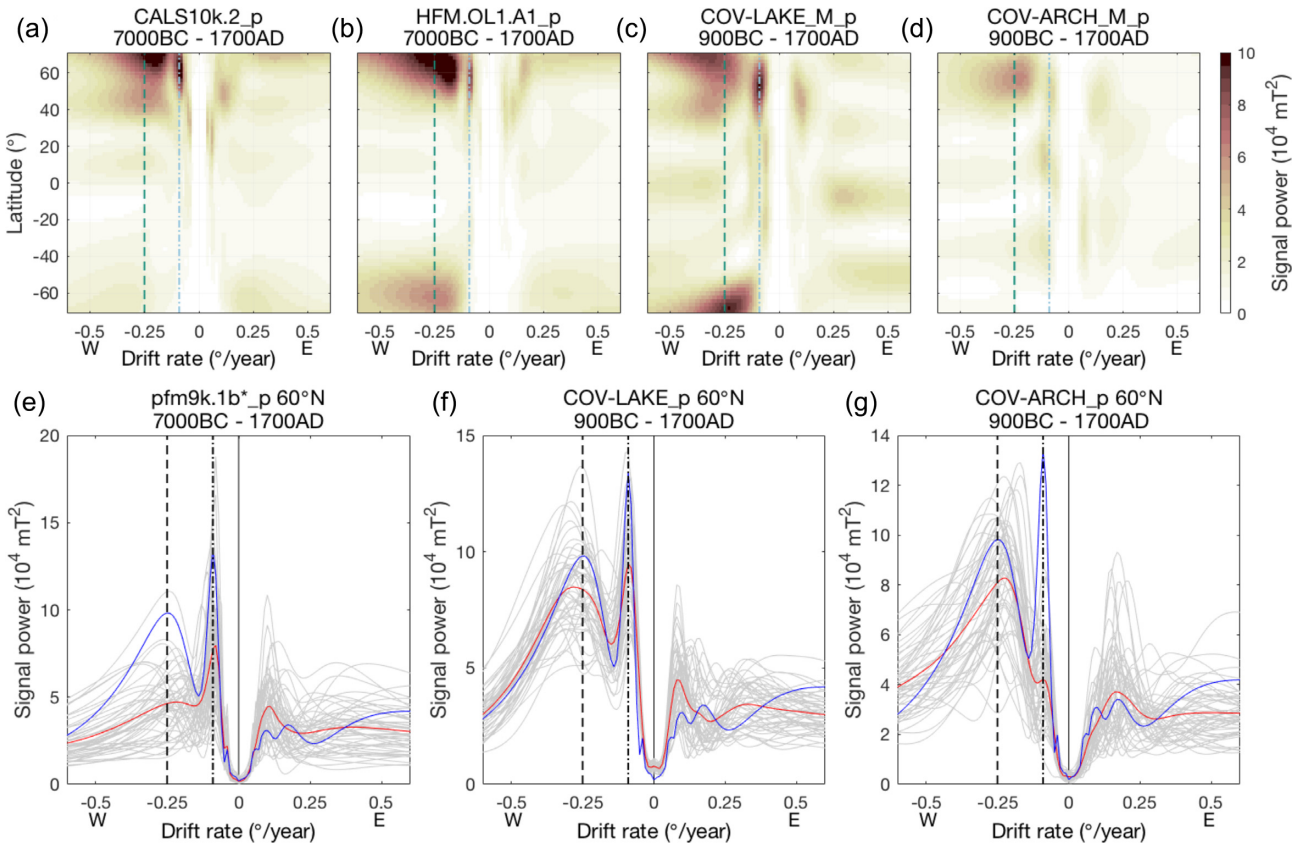

Figure 5. Upper panel: model comparison of Radon drift determinations on TL plot of (a) CALS10k.2_p and (b) HFM.OL1.A1_p over the time period 7000 BC–1700 AD and of (c) COV-LAKE_M_p and (d) COV-ARCH_M_p over the time period 900 BC–1700 AD. The suffix 'M' indicates that it is the mean model from an ensemble. All drift determinations were performed for latitudes 70° S to 70° N at 2° increments. The temporal and spatial resolution for each TL plot was 10 yr and 2°. Vertical green dashed and light blue dotted–dashed lines denote westward rift rates of $-0.25°$ and $-0.09°$ yr^{-1}, respectively. Lower panel: comparison of Radon drift determinations at 60° N between 50 randomly selected models (grey lines) from the same ensembles; (e) pfm9k.1b_p, (f) COV-LAKE_p and (g) COV-ARCH_p. The average signal (red line) and the drift determination of pfm9k.1a_p (blue line) are shown for reference. Vertical black dotted–dashed and dashed lines denote westward rift rates of $-0.09°$ and $-0.25°$ yr^{-1}, respectively. ∗For a more informative comparison the individual pfm9k.1b bootstrap models were remade using the same temporal damping that was used for pfm9k.1a, chosen to smooth out variations on timescales shorter than 300–400 yr (see Nilsson *et al.* 2014).

with an envelope wave propagating eastward with a group velocity ($v_g = \frac{\Delta\omega}{\Delta m}$) of 0.07° yr^{-1}. Constructive interference appears as an intensification of positive residual flux where the drift lines intersect in Fig. 1. The time interval t_c and longitudinal offset $\phi_c = v_g\ t_c$ between these points is calculated by setting $W\ (\phi_c, t_c) = 2\pi$ for one of the two inferred waveforms, which yields $t_c =$ 1125 yr and ϕ_c corresponding to 79°. The resultant interference pattern could be described as an eastward propagating beat frequency of 1/1125 yr^{-1}.

When we compare this to the unfiltered radial field at 60° N at the CMB (Fig. 6a), we find that this interference pattern coincides, both in terms of timing and location, with the three high-latitude weak/reverse flux patches previously noted by Nilsson *et al.* (2014). A similar pattern is also observed in other models (see Figs S3–S5, Supporting Information), although the fine-scale structure differs. To facilitate the comparisons, we have drawn yellow contour lines around what we (slightly arbitrarily) have defined as weak/reverse flux, weak flux corresponding to absolute B_r below a certain threshold ($|B_r| \leq 0.25|B_r|_{\mathrm{MAX}}$, where $|B_r|_{\mathrm{MAX}}$ is defined over the whole CMB). As noted by Nilsson *et al.* (2014), the high-latitude weak/reverse flux patches appear to originate from lower latitudes and migrate northwards. This suggests an important meridional component potentially related to something similar to the eccentric planetary-scale gyre observed in recent core-flow inversion (e.g. Pais & Jault 2008; Gillet *et al.* 2015)

To better quantify the occurrence of high-latitude weak/reverse flux we calculated the area of the core at latitudes greater than 45° N covered by weak/reverse flux. The results, shown in Fig. 6(b), confirm that the occurrence of high-latitude weak/reverse flux is generally consistent with the inferred 1125-yr periodicity signal over the past three millennia, that is with maximum extents of 20–40 per cent coinciding with the appearance of the three high-latitude weak/reverse flux patches previously mentioned, followed by relatively quiet periods in between. We note that the maximum extents of weak/reverse flux are generally lower for the models based on palaeomagnetic data compared to *gufm1*. However, the results are consistent if we compare to *gufm1* truncated at spherical degrees 5–6, suggesting that the difference is due to the lower spatial resolution of the palaeomagnetic models (see Nilsson *et al.* 2014).

4.3 Millennial-scale periodicity in the geomagnetic field

A millennial-scale periodicity signal (∼1350 yr), similar to the 1125-yr signal inferred from the interference pattern, has previously

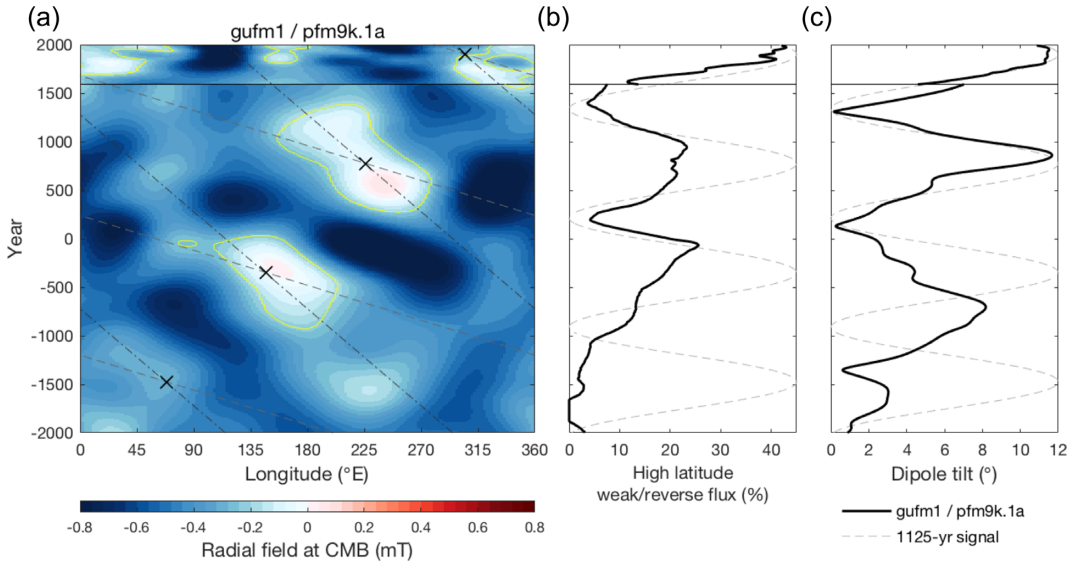

Figure 6. TL plots at 60° N of radial field at the CMB predicted by (a) *gufm1* (1590–1990 AD) and pfm9k.1a (2000 BC–1590 AD). Solid yellow lines denote areas with weak/reverse flux (for details see the main text). Dotted–dashed diagonal grey lines correspond to westward drift at rates of $-0.09^\circ\,\mathrm{yr}^{-1}$ ($f = -1/2000\ \mathrm{yr}^{-1}$, $m = 2$), dashed grey lines correspond to drift rates of $-0.25^\circ\,\mathrm{yr}^{-1}$ ($f = -1/1440\ \mathrm{yr}^{-1}$, $m = 1$) and black crosses mark the time and longitude of constructive interference between the two waveforms. Model comparison of (b) high-latitude weak/reverse flux occurrence calculated as the area of the core above 45° N latitude covered by weak/reverse flux (see the main text for details), (c) dipole tilt variations. The dashed grey lines (b) and (c) shows the 1125-periodicity signal (arbitrarily scaled amplitude) resulting from the interference pattern of inferred waveforms with peak values coinciding with crosses in (a).

been identified in dipole tilt variations over the past 9000 yr (Korte *et al.* 2011; Nilsson *et al.* 2011). Fig. 6(c) shows that the changes in dipole tilt are mostly in phase with the predicted periodicity signal, with large tilt angles coinciding with occurrence of high-latitude weak/reverse flux in the Northern Hemisphere. The agreement with the predicted periodicity signal becomes poorer the further back in time ones goes as the density of data decrease.

Interpretations of the observed westward drift in terms of high-latitude convection rolls and/or magnetic Rossby waves imply a largely antisymmetric field with respect to the equator. If these interpretations are correct, we may expect to find concentrations of weak or reverse field at high southern latitudes at similar times and longitudes where these are observed in the Northern Hemisphere (Fig. 6a). This is consistent with the more or less antisymmetric appearance and poleward migration of reverse flux patches in the Atlantic hemisphere associated with the development of the SAA, previously noted by Campuzano *et al.* (2019). In fact, the present field with SAA related to both high-latitude reverse flux at the CMB and a strong equatorial dipole (Amit & Olson 2008) might provide a good analogue of previous periods large dipole tilt over the past three millennia. However, while the growth of the SAA has been associated with a 9 per cent drop in the axial dipole field, potentially driven by the poleward migration of the reverse flux (Gubbins 1987; Finlay *et al.* 2016), we do not see any similar changes in dipole field in current models during the proposed analogues in the past.

5 CONCLUSIONS

Through analyses on TL plots of the geomagnetic field model pfm9k.1a, filtered to remove quasi-stationary field structures, we have found evidence for persistent and dominant westward drift at high latitudes of the CMB over the past 9000 yr. At high northern latitudes, we identify two distinct drift rates of -0.09° and $-0.25^\circ\,\mathrm{yr}^{-1}$ with dominant zonal wavenumbers $m = 2$ and 1, respectively, both of which are present over the past 3–4 millennia. Comparisons with other geomagnetic field models that include sedimentary data show similar westward drift signals over the same time period. Constructive interference between two westward propagating waveforms, inferred from these observations, predicts the recurrence of high-latitude weak/reverse flux every ∼1125 yr with a longitudinal offset of approximately 80° to the east from the previous occurrence. These predictions are largely in agreement with model observations over the same time period. In addition, the predicted 1125-yr periodicity signal is positively correlated with variations in the dipole tilt over the past three millennia. We speculate that the two identified drift signals could be related to the westward motion of high-latitude convection rolls and/or magnetic Rossby waves, originally proposed by Hide (1966). The detection of such waves in Earth's core could provide important constraints on the strength of the otherwise hidden toroidal part of the geomagnetic field (e.g. Hori *et al.* 2015). Improved model resolution at high northern and southern latitudes of the core would help to distinguish the proposed underlying processes, for example through further investigation into the dispersion relation, if a potential $m = 3$ signal can be resolved, and the proposed equatorial antisymmetry of the detected signals.

ACKNOWLEDGEMENTS

We would like to thank both Chris Finlay and Kumiko Hori for valuable discussions on the interpretation of our results as well as two anonymous reviewers whose comments considerably improved the manuscript. This work was partially funded by the Natural Environment Research Council, UK (grant number NE/I013873/1) and Swedish Research Council (grant number 2014–4125).

REFERENCES

Amit, H., Korte, M., Aubert, J., Constable, C. & Hulot, G., 2011. The time-dependence of intense archeomagnetic flux patches, *J. geophys. Res.: Solid Earth,* **116,** B12106, 10.1029/2011JB008538.

Amit, H. & Olson, P., 2008. Geomagnetic dipole tilt changes induced by core flow, *Phys. Earth planet. Inter.,* **166,** 226–238.

Arneitz, P., Egli, R., Leonhardt, R. & Fabian, K., 2019. A Bayesian iterative geomagnetic model with universal data input: self-consistent spherical harmonic evolution for the geomagnetic field over the last 4000 years, *Phys. Earth planet. Inter.,* **290,** 57–75.

Aubert, J., Finlay, C.C. & Fournier, A., 2013. Bottom-up control of geomagnetic secular variation by the Earth/'s inner core, *Nature,* **502,** 219–223.

Barrois, O., Hammer, M.D., Finlay, C.C., Martin, Y. & Gillet, N., 2018. Assimilation of ground and satellite magnetic measurements: inference of core surface magnetic and velocity field changes, *Geophys. J. Int.,* **215,** 695–712.

Bloxham, J. & Gubbins, D., 1985. The secular variation of Earth's magnetic field, *Nature,* **317,** 777–781.

Brown, M., *et al.*, 2015. GEOMAGIA50.v3: 2. A new paleomagnetic database for lake and marine sediments, *Earth Planet Space,* **67,** 1–19.

Bullard, E.C., Freedman, C., Gellman, H. & Nixon, J., 1950. The westward drift of the Earth's magnetic field, *Philos. Trans. R. Soc. Lond. A,* **243,** 67–92.

Campuzano, S., Gómez-Paccard, M., Pavón-Carrasco, F. & Osete, M., 2019. Emergence and evolution of the South Atlantic Anomaly revealed by the new paleomagnetic reconstruction SHAWQ2k, *Earth planet. Sci. Lett.,* **512,** 17–26.

Constable, C., Korte, M. & Panovska, S., 2016. Persistent high paleosecular variation activity in southern hemisphere for at least 10 000 years, *Earth planet. Sci. Lett.,* **453,** 78–86.

Dumberry, M. & Finlay, C.C., 2007. Eastward and westward drift of the Earth's magnetic field for the last three millennia, *Earth planet. Sci. Lett.,* **254,** 146–157.

Finlay, C.C., Aubert, J. & Gillet, N., 2016. Gyre-driven decay of the Earth/'s magnetic dipole, *Nat. Commun,* **7,** 10.1038/ncomms10422.

Finlay, C.C., Dumberry, M., Chulliat, A. & Pais, M.A., 2010. Short timescale core dynamics: theory and observations, *Space Sci. Rev.,* **155,** 177–218.

Finlay, C.C. & Jackson, A., 2003. Equatorially dominated magnetic field change at the surface of Earth's core, *Science,* **300,** 2084–2086.

Gillet, N., Jault, D. & Finlay, C.C., 2015. Planetary gyre, time-dependent eddies, torsional waves, and equatorial jets at the Earth's core surface, *J. geophys. Res.: Solid Earth,* **120,** 3991–4013.

Gubbins, D., 1987. Mechanism for geomagnetic polarity reversals, *Nature,* **326,** 167–169.

Gubbins, D. & Bloxham, J., 1987. Morphology of the geomagnetic field and implications for the geodynamo, *Nature,* **325,** 509–511.

Halley, E., 1692. An account of the cause of the change of the variation of the magnetical needle. with an hypothesis of the structure of the internal parts of the earth: as it was proposed to the Royal Society in one of their late meetings, *Philos. Trans. R. Soc. Lond.,* **17,** 563–578.

Hellio, G. & Gillet, N., 2018. Time-correlation-based regression of the geomagnetic field from archeological and sediment records, *Geophys. J. Int.,* **214,** 1585–1607.

Hide, R., 1966. Free hydromagnetic oscillations of the earth's core and the theory of the geomagnetic secular variation, *Philos. Trans. R. Soc. Lond. A,* **259,** 615–647.

Hori, K., Jones, C.A. & Teed, R.J., 2015. Slow magnetic Rossby waves in the Earth's core, *Geophys. Res. Lett.,* **42,** 6622–6629.

Hori, K., Teed, R.J. & Jones, C.A., 2018. The dynamics of magnetic Rossby waves in spherical dynamo simulations: a signature of strong-field dynamos?, *Phys. Earth planet. Inter.,* **276,** 68–85.

Korte, M., Constable, C., Donadini, F. & Holme, R., 2011. Reconstructing the Holocene geomagnetic field, *Earth planet. Sci. Lett.,* **312,** 497–505.

Korte, M., Donadini, F. & Constable, C.G., 2009. Geomagnetic field for 0–3 ka: 2. A new series of time-varying global models, *Geochem. Geophys. Geosyst.,* **10,** Q06008, doi:06010.01029/02008GC002297.

Korte, M., Genevey, A., Constable, C.G., Frank, U. & Schnepp, E., 2005. Continuous geomagnetic field models for the past 7 millennia: 1. A new global data compilation, *Geochem. Geophys. Geosyst.,* **6,** Q02H15, doi:10.1029/2004GC000800.

Livermore, P.W., Hollerbach, R. & Finlay, C.C., 2017. An accelerating high-latitude jet in Earth's core, *Nat. Geosci.,* **10,** 62–68.

Morrison, L.V. & Stephenson, F.R., 2001. Historical eclipses and the variability of the Earth's rotation, *J. Geodyn.,* **32,** 247–265.

Nilsson, A., Holme, R., Korte, M., Suttie, N. & Hill, M.J., 2014. Reconstructing Holocene geomagnetic field variation: new methods, models and implications, *Geophys. J. Int.,* **198,** 229–248, doi:210.1093/gji/ggu1120.

Nilsson, A., Muscheler, R. & Snowball, I., 2011. Millennial scale cyclicity in the geodynamo inferred from a dipole tilt reconstruction, *Earth planet. Sci. Lett.,* **311,** 299–305.

Nilsson, A., Suttie, N. & Hill, M.J., 2018. Short-Term Magnetic Field Variations From the Post-depositional Remanence of Lake Sediments, *Front. Earth Sci.,* **6,** doi: 10.3389/feart.2018.00039.

Pais, M.A. & Jault, D., 2008. Quasi-geostrophic flows responsible for the secular variation of the Earth's magnetic field, *Geophys. J. Int.,* **173,** 421–443.

Panovska, S., Korte, M., Finlay, C.C. & Constable, C.G., 2015. Limitations in paleomagnetic data and modelling techniques and their impact on Holocene geomagnetic field models, *Geophys. J. Int.,* **202,** 402–418.

Pavón-Carrasco, F.J., Osete, M.L., Torta, J.M. & De Santis, A., 2014. A geomagnetic field model for the Holocene based on archaeomagnetic and lava flow data, *Earth planet. Sci. Lett.,* **388,** 98–109.

Terra-Nova, F., Amit, H., Hartmann, G.A. & Trindade, R.I.F., 2015. The time dependence of reversed archeomagnetic flux patches, *J. geophys. Res.: Solid Earth,* **120,** 691–704.

Terra-Nova, F., Amit, H., Hartmann, G.A. & Trindade, R.I.F., 2016. Using archaeomagnetic field models to constrain the physics of the core: robustness and preferred locations of reversed flux patches, *Geophys. J. Int.,* **206,** 1890–1913.

Wardinski, I. & Korte, M., 2008. The evolution of the core-surface flow over the last seven thousands years, *J. geophys. Res.: Solid Earth,* **113,** B05101, 10.1029/2007JB005024.

Yoshida, S. & Hamano, Y., 1993. The westward drift of the geomagnetic field caused by length-of-day variation, and the topography of the core-mantle boundary, *Geophys. J. Int.,* **114,** 696–710.

SUPPORTING INFORMATION

Supplementary data are available at *GJI* online.

Figure S1. Percentage of the rms deviation from the pfm9k.1a time-averaged radial magnetic field (B_r) at the CMB captured by the residual field (RF) for different filter cut-off periods. Our preferred cut-off period of 2500 yr removes quasi-stationary features of the field while capturing 42 per cent of the rms variation seen in the original signal.

Figure S2. TL plots at 60° S of the radial field at the CMB predicted by (a) pfm9k.1a and (b) pfm9k.1a_p and at 60° N predicted by (c) pfm9k.1a[$l_{max} = 4$]_p (pfm9k.1a truncated at spherical harmonic degree 4). The first and last 300 yr of the filtered models (shaded grey area) were not considered during the analyses due to end-effects associated with the filtering process. Dotted–dashed diagonal grey lines correspond to westward drift at rates of $-0.09°\ \mathrm{yr}^{-1}$ ($f = -1/2000\ \mathrm{yr}^{-1}$, $m = 2$) and dashed grey lines correspond to drift rates of $-0.25°\ \mathrm{yr}^{-1}$ ($f = -1/1440\ \mathrm{yr}^{-1}$, $m = 1$).

Figure S3. TL plots at 60° N of the radial field at the CMB predicted by (a) CALS10k.2 (Constable *et al.* 2016) and (b) CALS10k.2_p, with the axisymmetric part of the field removed and high-pass filtered with cut-off frequency of $1/2500\ \mathrm{yr}^{-1}$. The first and last 300 yr of the filtered models (shaded grey area) were not considered during the analyses due to end-effects associated with the filtering process. Dotted–dashed diagonal grey lines correspond to westward drift at rates of $-0.09°\ \mathrm{yr}^{-1}$ ($f = -1/2000\ \mathrm{yr}^{-1}$, $m = 2$) and

dashed grey lines correspond to drift rates of $-0.25^\circ\,\mathrm{yr}^{-1}$ ($f = -1/1440\ \mathrm{yr}^{-1}$, $m = 1$). Also shown is the frequency–wavenumber spectra of TL plots based on CALS10k.2_p at 60° N over time periods (c) 2000 BC–1700 AD, (d) 5000–1000 BC, (e) 7000–4000 BC and (f) at 60° S over 2000 BC–1700 AD. The light blue stars, frequency $f = -1/2000\ \mathrm{yr}^{-1}$ and zonal wavenumber $m = 2$, and green stars, frequency $f = -1/1440\ \mathrm{yr}^{-1}$ and zonal wavenumber $m = 1$, are shown for reference only. Positive (negative) frequencies indicate eastward (westward) drift.

Figure S4. TL plots at 60° of the radial field at the CMB predicted by (a) HFM.OL1.A1 (Constable *et al.* 2016) and (b) HFM.OL1.A1_p, with the axisymmetric part of the field removed and high-pass filtered with cut-off frequency of $1/2500\ \mathrm{yr}^{-1}$. The first and last 300 yr of the filtered models (shaded grey area) were not considered during the analyses due to end-effects associated with the filtering process. Dotted–dashed diagonal grey lines correspond to westward drift at rates of $-0.09^\circ\,\mathrm{yr}^{-1}$ ($f = -1/2000\ \mathrm{yr}^{-1}$, $m = 2$) and dashed grey lines correspond to drift rates of $-0.25^\circ\,\mathrm{yr}^{-1}$ ($f = -1/1440\ \mathrm{yr}^{-1}$, $m = 1$). Also shown is the frequency–wavenumber spectra of TL plots based on HFM.OL1.A1_p at 60° N over time periods (c) 2000 BC–1700 AD, (d) 5000–1000 BC, (e) 7000–4000 BC and (f) at 60° S over 2000BC–1700AD. The light blue stars, frequency $f = -1/2000\ \mathrm{yr}^{-1}$ and zonal wavenumber $m = 2$, and green stars, frequency $f = -1/1440\ \mathrm{yr}^{-1}$ and zonal wavenumber $m = 1$, are shown for reference only. Positive (negative) frequencies indicate eastward (westward) drift.

Figure S5. TL plots at 60° N of the radial field at the CMB predicted by (a) COV-LAKE_M (Hellio & Gillet 2018), (b) COV-LAKE_M_p, (c) COV-ARCH_M (Hellio & Gillet 2018) and (d) COV-ARCH_M_p. The suffix 'M' indicates that it is the mean model from an ensemble. For the filtered models (suffix 'p') the axisymmetric part of the field removed and high-pass filtered with cut-off frequency of $1/2500\ \mathrm{yr}^{-1}$. The first and first and last 300 yr of the filtered models (shaded grey area) were not considered during the analyses due to end-effects associated with the filtering process. Dotteddashed diagonal grey lines correspond to westward drift at rates of $-0.09^\circ\,\mathrm{yr}^{-1}$ ($f = -1/2000\ \mathrm{yr}^{-1}$, $m = 2$) and dashed grey lines correspond to drift rates of $-0.25^\circ\,\mathrm{yr}^{-1}$ ($f = -1/1440\ \mathrm{yr}^{-1}$, $m = 1$). Also shown is the frequency–wavenumber spectra of TL plots over the period 900 BC–1700 AD based on COV-LAKE_M_p at (e) 60° N and (f) 60° S and based on COV-ARCH_M_p at (g) 60° N and (h) 60° S. The light blue stars, frequency $f = -1/2000\ \mathrm{yr}^{-1}$ and zonal wavenumber $m = 2$, and green stars, frequency $f = -1/1440\ \mathrm{yr}^{-1}$ and zonal wavenumber $m = 1$, are shown for reference only. Positive (negative) frequencies indicate eastward (westward) drift.